Mass Transport in Nanoporous Gold and Correlation with Surface Pores for EC 1 Mechanism: Case of Ascorbic Acid

Abhishek Kumar, Josue M Gonçalves, Vinicius L Furtado, Koiti Araki, Lucio Angnes, Marcel Bouvet, Mauro Bertotti, Rita Meunier-prest

Entry for the Table of Contents

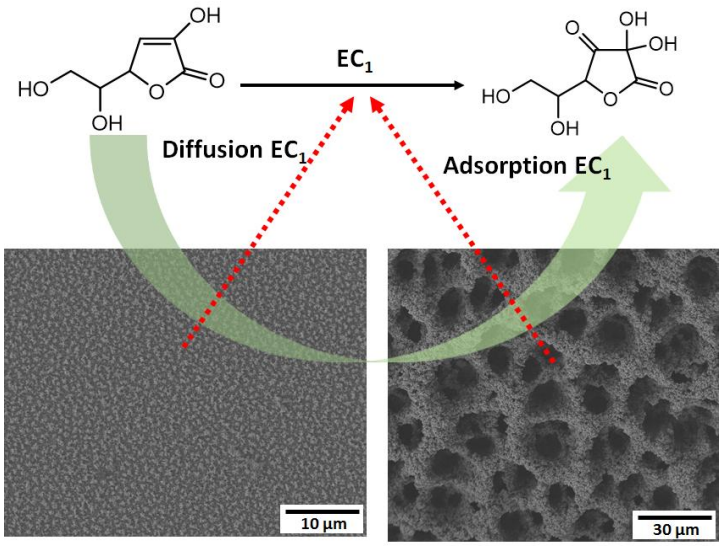

Playing with the pores: Surface pores size in nanoporous gold modulates the electrode reactions pathways of ascorbic acid. The reaction is largely driven by diffusion when pores are smaller (nanometer). On the contrary, adsorption holds the key role when pores are bigger (micrometer), allowing permeation of molecules in the film volume.

Mass transport in nanoporous gold and correlation with surface pores for EC_1 mechanism: Case of ascorbic acid

Dr. Abhishek Kumar*[a,b], Dr. Josue M. Gonçalves[b], Mr. Vinicius L. Furtado[b], Prof. Koiti Araki[b], Prof. Lucio Angnes[b], Prof. Marcel Bouvet[a], Prof. Mauro Bertotti [b], Dr. Rita Meunier-Prest*[a]

In Memoriam: Prof. Jean-Michel Savéant

[a] Institut de Chimie Moléculaire de l'Université de Bourgogne, UMR CNRS 6302, Université Bourgogne Franche-Comté, 9 Avenue Alain Savary, Dijon Cedex 21078, France
[b] Department of Fundamental Chemistry, Institute of Chemistry, University of São Paulo, Av. Prof. Lineu Prestes, 748, 05508-000 São Paulo, SP, Brazil

Email: rita.meunier-prest@u-bourgogne.fr, Abhishek.Kumar@u-bourgogne.fr

Supporting information for this article is given via a link at the end of the document.

Abstract: The present work correlates the mass transport of ascorbic acid (AA), which undergoes an electrochemical reaction accompanied by a first-order chemical reaction (EC_1 mechanism), with the size of surface pores of nanoporous gold (NPG) films. NPG films were electrodeposited on gold microelectrodes, generating polycrystalline, and highly porous surfaces. Studies of AA electrooxidation reveal mainly diffusional mass transport driven by EC_1 pathways on the NPG electrodes prepared by changing the deposition potential. Similar studies on the NPGs prepared by changing the deposition time exhibit mainly diffusional transport at shorter deposition times, and largely an adsorption process driven by EC_1 at longer deposition times. Such transition in the reaction pathways from *diffusion* EC_1 to *adsorption* EC_1 is correlated with the evolution of micrometer large surface pores in NPG films prepared at longer deposition times, allowing the diffusion of AA from the bulk solution to the volume of NPG, which enhances the adsorption probability.

Introduction

Among different classes of nanomaterials, porous nanostructures have attracted wide research interests and promise to usher remarkable advancements in the conventional electroanalytical techniques and electrocatalysis processes. For instance, highly ordered 2D and 3D films of metal and molecularly imprinted polymers having inverse opal geometry were electrochemically synthesized using hierarchical templating from colloidal solutions and demonstrated very high sensitivity to detect human serum albumin.[1] Highly ordered thin films of silica and related mesoporous hybrids were extensively studied for diverse electrochemical analysis.[2] An ultrathin 2D mesoporous networks of Iridium nanosheets was synthesized using close-packed array of soft polymeric micelle templates and demonstrated high electrocatalytic activities in oxygen evolution reactions.[3] Nanoporous gold (NPG) is another intensively studied nanostructured materials, stimulating researches in a plethora of electrochemical applications areas.[4] The basic structural architecture of NPG is described by an interconnected network of nanometric struts and pores,[5] whose extended morphology varies depending on the top-down and bottom-up synthesis procedures. Chemical and electrochemical dealloying of a gold-containing alloy with a less noble metal (Ag, Cu, Zn) is among the most followed top-down approaches to obtain a homogenous NPG film with similar-sized nanopores and struts commonly called ligaments.[6] Template-assisted electrodeposition from a gold-containing precursor solution is another strategy (bottom-up)[7] that has gained relevance in recent years. NPG films realized through this method resulted in a multiplicity of pore sizes and strut features, usually grown in the form of fractals.[8] The different NPG synthesis approaches are strongly correlated with their structural features and influence their electrochemical properties. The high NPG electrochemical activity was previously attributed mainly to the enhanced surface area,[9] but later researchers confirmed that the exposure of specific crystalline facets[10], atomic-scale structural defects[11] and the nanoconfinement phenomenon[12] have also relevance to explain the electrocatalytic properties. Such versatile properties of NPG materials inspired researchers to design diverse and innovative electroanalytical platforms to detect several analytes such as nitrite,[8, 13] dopamine (DA),[14] glucose,[15] uric acid (UA),[16] ascorbic acid (AA),[17] among others, with high sensitivity, low detection limit, and unique selectivity.

Ascorbic acid is an antioxidant, which performs many important functions in cellular redox metabolism and is also used in food and pharmaceutical industries.[18] Its optimum concentration in biofluids is considered as a benchmark of health well-being, reinforcing the importance of AA monitoring and selective quantification. Taking into account its electrochemical activity, electroanalytical approaches have shown clear advantages over other methods in terms of their excellent sensitivity, simplicity, electronic integration, low cost and miniaturization.[19] Traditionally, uncoated metal[20] and carbon electrodes[21] have been used to assess AA in different matrices, but these electrodes suffer from slow kinetics and interferences from dopamine and uric acid, which are also oxidized at similar potentials. An approach to overcome these limitations is using single-crystal gold electrodes,[22] which significantly shift the AA electrooxidation peak away from those of DA and UA, thereby preventing their interferences. However, on such electrodes the oxidation product of AA is strongly adsorbed, thus reducing the durability and reproducibility of the sensor. Nanostructuring of these conventional electrodes with diverse nanomaterials such as carbon nanotubes,[23] metal nanoparticles,[24] and metal-organic nanocomposites[25] are another alternative to improve the AA sensing performance. Thin NPG films deposited over gold and carbon electrodes have been recently investigated for voltammetric[26] and amperometric detection of AA.[17] These studies demonstrated that the coating

of conventional electrodes with NPG films is a useful approach to enhance the sensitivity towards AA detection, which is expected owing to the very high NPG surface area. Moreover, a strong electrocatalytic effect has also been noticed in our recent works on NPG electrodes as a consequence of the faster electron-transfer kinetics, with a remarkable shift of the AA electrooxidation peak towards less positive potential values.[27] These studies revealed that electrocatalysis depends on the NPG film structural features, particularly pore sizes and Au crystallographic orientation. Thus, it is expected that mass transport in the AA electrochemical process strongly depends on the NPG morphology and a clear understanding of such features is pertinent for designing advanced electroanalytical platforms for AA detection.

Studies on mass transport in NPG materials are still in infancy, and new experimental as well as theoretical reports are coming out to unravel this phenomenon. Until now, a broader consensus is that mass transport is limited through nanoporous films such that permeation of analytes in the deeper pores is restricted[28] during the electrode polarization. This has also been demonstrated in the recent work of Veselinovic et al., according to which the sensitivity for nucleic acid detection was not linearly proportional to the NPG electrochemical surface area (ECSA).[29] Therefore, a trade-off between mass transport limitation and ECSA is always noticed to improve the electroanalytical performance of NPG-based platforms.[30] This balance depends on two important factors: the kinetics and mechanism of the electrode reactions, and the pore size in the NPG films. At first, electrode reactions with slower kinetics are expected to have lower mass transport limitations because the analyte would have a longer time to travel deeper in the film before getting oxidized/reduced. On the other hand, larger pore sizes such as in micrometer dimensions are expected to reduce mass transport limitations. Beside these, other approaches of mass transport enhancement in mesoporous silica thin films were reported through faster charge transfer reactions by using neutral or cationic redox mediator.[31] In the case of AA electrooxidation on NPG microelectrodes, the reaction mechanism of AA is expected to vary, owing to the changes in mass transport limitations at films with different morphologies. Therefore, the AA reaction mechanism on different types of NPG surfaces and its correlation with the mass transport will be key to maximize the NPG area utilization and thus designing high-performance AA electroanalytical platforms.

In this context, herein we present a systematic investigation of the AA electrochemical process at different NPG surfaces, which is further correlated with the structural features of the NPG films. Thin NPG films were electrodeposited on Au microelectrodes by the dynamic hydrogen bubble template (DHBT) method[32] using a gold precursor solution. In this method, the evolution of hydrogen bubbles at the electrode imparts a dynamic template to the co-deposition of gold atoms, inducing porosity in the deposited film. The NPG films were prepared by systematically varying the electrodeposition conditions, such as deposition potential (E_D) and time (t_D). The NPG films were characterized by electron microscopies, XRD, and cyclic voltammetry (CV) to unravel their morphologies, crystalline microstructures and electrochemical surface area. Electrochemical processes of AA on different NPG microelectrodes were studied by CV. A systematic study of mass transport was performed by changing the scan rate and the AA concentration in a wide range, and the results were correlated with the AA redox process mechanism. These were subsequently interlinked with the structural features such as pore sizes of the NPG prepared at different electrodeposition conditions.

Results and Discussion

Electrochemical, morphological, and structural characterizations of NPG. The formation of NPG films on gold microelectrodes was confirmed by comparing the CVs of the modified and bare gold microelectrodes in 0.5 mol L^{-1} H_2SO_4 at 50 mV s^{-1} in the range of 0.2 V to 1.6 V. The voltammogram shown in Fig. 1 depicts three anodic peaks for the NPG modified microelectrode. These peaks are associated with the oxidation of gold at different crystalline facets into gold oxides, and the reduction wave centered between 0.8 to 0.9 V is attributed to the regeneration of metallic gold after being oxidized in the positive scan. The oxidation peaks at ca. 1.20 V, 1.30 V, and 1.44 V correspond to the (220) (200) and (111) crystalline planes of gold in NPG films.[33] The evolution of low-indexed Au-planes in NPG films and the enhancement in its proportion with increasing t_D were also previously reported.[27, 34]

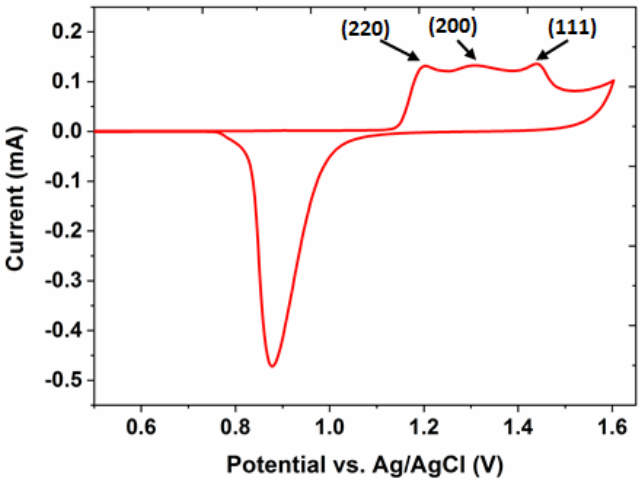

Figure 1. Voltammogram recorded with an NPG microelectrode prepared at E_D = -4 V and t_D = 400 s in 0.5 mol L^{-1} H_2SO_4 solution at 50 mV s^{-1}.

Similar voltammograms of NPG modified gold microelectrodes prepared at different E_D (from -1 to -4 V) for a fixed t_D (100 s) and a fixed E_D of -4 V for different t_D (50 to 600 s) were recorded at similar conditions (Fig. S1). It can also be noticed that the charge associated with both oxidation and reduction processes is higher for NPG microelectrodes compared to that of bare gold microelectrodes, confirming the enhancement of the ECSA because of the film nano structuration. The ECSA values for different NPG films were determined by integrating the gold oxide reduction peak for each CV (Fig. S2) and the results are given in Table S1. An exponential increase in ECSA values as a function of t_D was observed, whereas a linear increase was found with changing E_D (Fig. S3).

The implication of electrodeposition parameters on NPG film morphology is evident in the Scanning Electron Microscopy (SEM) micrographs presented in Fig. 2. NPG films deposited for up to 100 s resemble the top view of a grove with spaced trees formed by gold clusters. The morphology is in agreement with the recently reported atomic-scale growth model [35] as well as the classical theory of Diffusion Limited Aggregation (DLA),[36] in which the gold atoms generated upon reduction at the gold microelectrode surface, diffuses back and aggregates at the nucleation centers. As t_D increases, the canopies tend to enlarge and come together generating a more compact surface (t_D = 200 s, Fig. 2b), until the entrapped hydrogen bubbles become bigger (small bubbles coalesce to form larger ones) and eventually burst out changing completely the NPG film morphology (t_D = 400 s, Fig. 2c). Accordingly, the film now exhibits larger pores separated by thicker walls and becomes thicker and thicker, finally exhibiting a sponge like morphology with interconnected walls (pores diameters in the 10 to 25 µm range) characteristic of NPG prepared by DHBT at t_D = *600 s and longer*. Such phenomenon is clearly evidenced by the sequence of SEM image of NPG film as a function of deposition time (E_D = -4 V) depicted in Figure 2. In contrast, such a dramatic morphologic change was not observed by varying E_D from -1 to -4 V while t_D was fixed in 100 s (Fig. S4). In this case, the surface is first densely covered by small aggregates of gold clusters, that tend to grow up and evolve to the spaced trees morphology as E_D is made more negative.

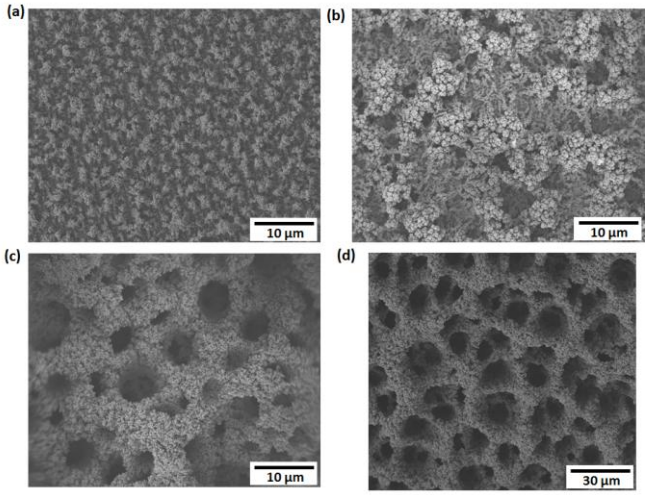

Figure 2. SEM images of NPG films prepared on a gold substrate at a fixed E_D = -4 V and for different t_D: 100 s (a), 200 s (b), 400 s (c), and 600 s (d).

The micrometric porous walls also depict a range of nanometric structures, which changes as a function of deposition conditions (Fig. S5). For NPG films deposited at -4 V for 600 s, the wall is composed of porous 3D dendrite fractals (pores are marked in red circles) on the nanometric scale (Fig. 3a). These dendrites display a few hundred nm long trunk and secondary and tertiary branching, in agreement with the DLA growth profile. Such porous dendritic nanostructures are also expected to enhance the rate of electrochemical reactions and thus the sensitivity of the modified electrodes, as demonstrated recently, [37] Since the NPG films were synthesized from $HAuCl_4$ solution, there is a possibility of chloride adsorption from the precursor solution, and such speculation was investigated by X-ray Photoelectron Spectroscopy (XPS) elemental analysis. The XPS survey spectrum of the NPG film (Fig. 3b) reveals mainly the characteristics Au peaks at 84, 335.2, 353.6, 546, 642.4 and 761 eV, assigned to different electronic shells of Au. The presence of chlorine was also ruled by recording a high-resolution Cl2p spectum (Fig. S6), showing absence of any peak for Cl and ruling out any contamination from chloride during the deposition process.

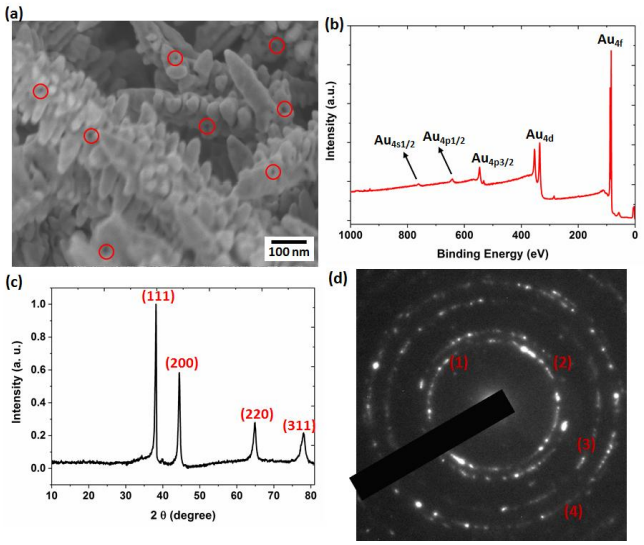

Figure 3. Magnified SEM image (a), XPS profile (b), background-corrected XRD pattern (c), and SAED pattern obtained in HRTEM imaging (d) of the NPG film electrodeposited on a gold substrate at an applied potential of -4 V for 600 s.

The crystalline microstructure and the orientation of gold atoms in the NPG film were assessed by XRD (Fig. 3c) and SAED patterns performed in HRTEM imaging (Fig. 3d). The diffraction pattern revealed a gold polycrystalline film with characteristic reflections at 38.2°, 44.5°, 64.8°, and 78.0°, assigned to (111), (200), (220), and (311) planes of the fcc lattice of gold, respectively [JCPDS 04-0784].[38] The evolution of intense reflection peaks associated with low indexed planes also corroborates with the multiple oxidation peaks observed in the NPG film CV (Fig. 1). The results observed in the XRD pattern were further confirmed by the SAED pattern, which displays four concentric rings named (1), (2), (3), and (4), each one being originated from the electron diffraction from a specific crystallographic gold orientation (Figure 3d). The diameter of each ring corresponds to the interplanar distance of the associated plane in the lattice, and the values are in close agreement with those estimated by XRD.

Electrochemical process of AA on NPG surface. The electrochemical behavior of AA was investigated on two different sets of NPG microelectrodes prepared at varying applied potentials for a fixed deposition time and vice versa. CV curves were recorded in the range of -0.3 V to 0.6 V in PBS buffer in a broad concentration and scan rate ranges. The voltammograms of NPG microelectrodes (Fig. 4a and 4b) consist of sharp anodic

waves corresponding to the oxidation of AA into dehydroascorbic acid (DHA),[39] peaking near 0 V in contrast to a relatively much slower and non-steady-state wave obtained at the bare electrode (Fig. 4c). It is evident from the large negative shift and the steepness of the oxidation waves that AA experiences electrocatalysis and faster electron transfer kinetics at all the NPG electrodes. However, the shape of the voltammograms changes as a function of E_D and t_D parameters employed for the NPG synthesis. For the NPGs prepared at different E_D values, the AA oxidation voltammograms are non-symmetric, typical of a diffusional process. Moreover, the peaks are broad and poorly defined, which can be attributed to the partial microelectrode feature in which radial diffusion plays an important role in mass transport. Because of that, a steady-state current is obtained because of the effective material flux toward the electrode. Additionally, the peak current density (calculated by dividing current by ECSA for each NPG microelectrode, as given in Table S1) decreases as E_D changes from -1 V to -2 V, and remains constant thereafter, while the electrode area increases linearly as the E_D is made more negative (Fig. S.3a). This indicates that a larger fraction of the NPG surface remains inaccessible to AA, even for thicker films prepared at more negative applied potentials.

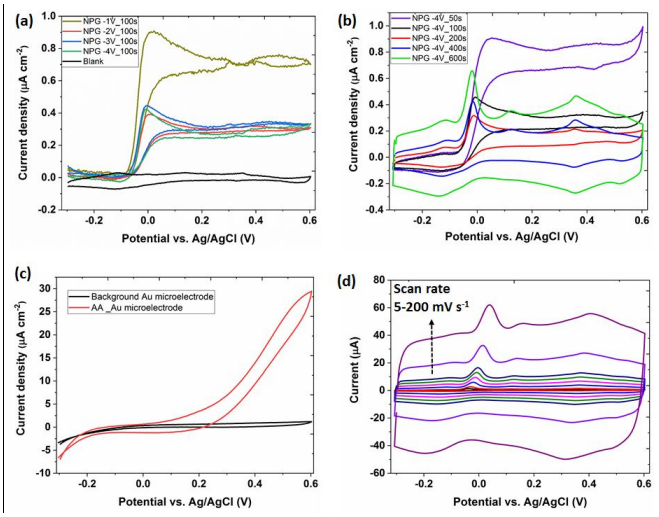

Figure 4. Voltammograms recorded in 0.5 mmol L^{-1} AA + 0.1 M PBS at scan rate of 20 mV s^{-1} with NPG microelectrodes prepared at different E_D for a fixed t_D (100 s) (a) and at a fixed E_D (-4 V) for different t_D (b). CVs of the bare gold microelectrode in the presence and absence of AA (c) and CVs of the NPG microelectrode (-4 V for 600 s) recorded at different scan rates in 0.5 mmol L^{-1} AA + 0.1 mol L^{-1} PBS (d).

The AA oxidation at the NPG surfaces prepared at different t_D presented a more diverse scenario, in which the voltammograms underwent a systematic transition from non-symmetric to symmetric peak as a function of increasing t_D. As depicted in Fig. 4b, the CV obtained for an NPG prepared at t_D = 50 s exhibited an S-shaped anodic peak with steady-state oxidation current, characteristics of radial diffusion. Interestingly, the sigmoidal voltammetric curve at first is converted into a broad peak (for 100 and 200 s), characteristics of planar diffusion, then to a completely symmetric wave (for 400 and 600 s), typical of an adsorption process. Notably, larger capacitive currents are noticed for NPG microelectrodes prepared at longer t_D values, which is attributed to thicker films with an enhanced surface area. Thus, the deposition time in the NPG synthesis strongly influences the voltammetric behavior of AA as a consequence of a change in the mass transport regime, while such effect is not observed by changes in the deposition potential.

The effect of scan rate on the voltammograms corresponding to the anodic oxidation of AA was investigated for all NPG microelectrodes. Figure 4d shows such CV curves recorded in the range of 5 to 200 mV s^{-1} for an NPG film prepared at a fixed E_D of -4 V for t_D = 600 s. An increase in capacitive as well as Faradaic current is noticed as a function of scan rate. To extract more information about such electrochemical process, peak potential (E_p) and peak current (i_p) values were plotted as a function of log (scan rate) (log v) for different NPG microelectrodes.

Mass transport of AA at different NPG surfaces. The mechanism concerning the AA anodic oxidation has been previously reported as a 2 electrons, 2 protons electrochemical reaction (E) accompanied by a fast first-order hydration reaction of DHA (C_1),[39] referred to as EC_1 process. At the NPG surface, we propose that a combination of diffusion and adsorption processes takes place, named *diffusion EC_1* and *adsorption EC_1*. The first mechanistic study of such *diffusion/adsorption EC_1* processes was proposed by E. Laviron,[40] and based on that, an electrode reaction scheme for the AA oxidation can be rationalized, as depicted in Fig. 5.

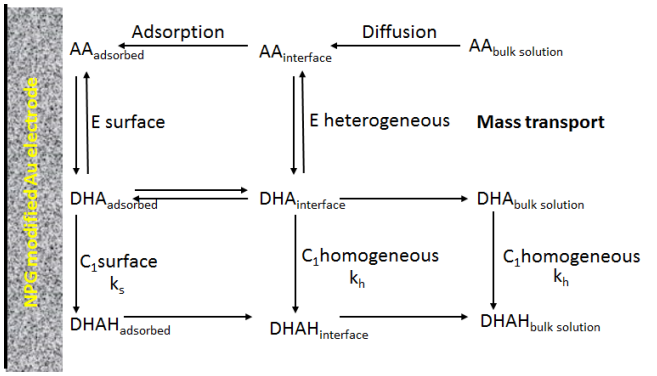

Figure 5. The general reaction scheme of AA oxidation through an EC_1 process.

The scheme starts with the diffusional transport of AA from the bulk solution towards the electrode/electrolyte interface, where it can either undergo heterogeneous electrochemical oxidation through the loss of two electrons and two protons to form DHA, or it can be adsorbed on the NPG surface. In the former case, the DHA species is further converted into its hydrated form DHAH through a homogeneous chemical reaction in the solution close to the NPG surface, which is transported away from the interface to the bulk solution. In the latter case, the adsorbed AA is electrochemically oxidized into adsorbed DHA, which can either remain adsorbed on the surface and undergoes surface hydration or diffuse to the electrode/electrolyte interface in the solution and undergoes a homogeneous chemical reaction to form the final product DHAH.

The nature of the chemical reaction (surface or homogeneous) is difficult to establish. In some cases, Savéant showed that the

homogeneous chemical reaction could present a surface reaction feature.[41] This is particularly true when the thickness of the reaction layer becomes of the same order asf the molecule dimensions. For the *adsorption EC$_1$* process, the variation of peak potential with the scan rate is described by the Laviron equation [42], as given by equation (1). In this equation, E_p is the anodic peak potential, $E^{0\prime}$ the surface standard potential, k_s the surface chemical reaction constant, v the scan rate, and n the number of electrons involved in the faradaic process, while other symbols are standard electrochemical parameters. It is evident from the equation that E_p is linearly related to *log v* with a slope of 2.3RT/nF. Taking n equals 2 for the AA EC$_1$ process occurring with an adsorbed species, the slope is 0.029 V for the *adsorption EC$_1$ process*.

$$E_p = E^{0\prime} - \frac{2.3RT}{nF} log \frac{RTk_s}{nFv} \quad (1)$$

On the other hand, the variation of peak potential with scan rate for a *diffusion EC$_1$ process* is described by the equation (2), which was proposed by R. Nicholson[43] and J. M. Saveant.[44] In equation (2), E_p is the anodic peak potential, E^0 the heterogeneous standard potential, and k_h the homogeneous chemical reaction constant. According to this equation, E_p is linearly related to *log v* with a slope of half that of a surface process (2.3RT/2nF), which becomes 0.015 V for the AA *diffusion EC$_1$* process.

$$E_p = E^0 - \frac{2.3RT}{2nF} log \frac{0.21RTk_h}{nFv} \quad (2)$$

The peak current (i_p) is also uniquely correlated with the scan rate in an EC$_1$ process controlled by diffusion or adsorption, such that *log* i_p changes linearly with *log v* with a slope of 0.5 for a *diffusion EC$_1$* mechanism and 1 for an *adsorption EC$_1$* mechanism, as discussed in detail in the recent Saveant´s book.[45]

Accordingly, changes of E_p (or $E_{1/2}$) and i_p with the scan rate toward the AA electrooxidation were examined for two different sets of aforementioned NPG microelectrodes. Fig. 6a shows the variation of E_p and $E_{1/2}$ vs. *log v* for voltammograms recorded with NPG microelectrodes prepared at different applied potentials for a fixed deposition time. At low scan rates, $E_{1/2}$ is obtained and is independent of the scan rate. It reveals the microelectrode mass transport feature because of radial diffusion, and this behavior can be confirmed from the CV curves recorded at a low scan rate (Fig. 4a), which exhibit a sigmoidal profile instead of a peak. However, at higher scan rates, E_p changes linearly with *log v*, with approximately the same slope values (0.015-0.019 V) obtained at all the studied NPG microelectrodes, a characteristic of a *diffusion EC$_1$* process. This is further corroborated by the logarithmic plots of i_p vs. scan rate shown in Fig. 6b, which shows a linear relationship between *log* i_p and *log v,* with slopes ranging between 0.5 to 0.6, typical of a diffusional process. Therefore, these results confirm that the AA anodic oxidation is predominantly driven by *diffusion EC$_1$* behavior at all NPG microelectrodes prepared at different E_D values for a fixed t_D of 100 s. This can also be correlated with the NPG structural features, particularly the pore size. As shown in Fig. S4, the morphology of all NPG surfaces remains similar in terms of pore size, presenting a relatively dense packing of gold nanocrystals with smaller pores in the range of nanometers. Therefore, AA diffusing from bulk solution is more likely to stay on the surface and less likely to enter the NPG film volume because it is quickly oxidized on the surface owing to the relatively faster heterogeneous electron transfer kinetics [27]. Such mass transport limitation regarding electrochemical processes on NPG films with small pore size has already been reported [29-30].

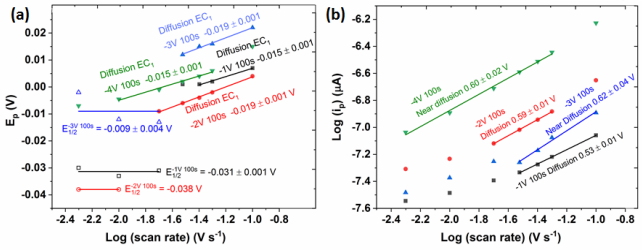

Figure 6. Plots of E_p vs. log (scan rate) (a) and log (i_p) vs. log (scan rate) (b), extracted from CVs recorded in 0.1 mmol L^{-1} AA + 0.1 mol L^{-1} PBS in the scan rate range of 5-200 mV s^{-1} with NPG microelectrodes prepared at different E_D (-1 V, -2 V, -3 V and -4 V) for a fixed t_D (100 s). Slopes are indicated in the graph.

Interestingly, a different behavior was noticed in similar plots obtained for the AA electrode process for NPG films prepared at a fixed E_D (-4 V) but for varying t_D (in the range of 50 to 600 s) (Fig. 7). At the shorter t_D value (50 s), $E_{1/2}$ is reported instead of E_p because the voltammogram recorded with this electrode presented a steady-state feature instead of a peak-shaped profile. Moreover, it is also evident that $E_{1/2}$ remains independent of the scan rate, which is the typical case of radial diffusion for a microelectrode. As t_D increases, a more prominent peak is observed, which indicates the prevalence of planar diffusion over radial diffusion. Voltammograms recorded with such NPG microelectrodes present a peak, and E_p changes linearly with log v, but the slope value changes as a function of t_D. For t_D = 100 s, the slope is ca. 0.016 V, characteristics of a *diffusion EC$_1$* process. For t_D = 200 s, two different slopes are obtained, one at low scan rates characteristics of a *diffusion EC$_1$* process (0.015 V), and another at higher scan rates corresponding to an *adsorption EC$_1$* process (0.030 V). For the other NPG microelectrodes prepared at longer deposition times, the linear relationship yielded a single slope of ca. 0.030 V, indicating that an *adsorption EC$_1$* process takes place for all scan rates. A transition from a *diffusion EC$_1$* to an *adsorption EC$_1$* process for NPG microelectrodes prepared at 200 s is noted in Fig. 7b, which shows results on the variation of *log* i_p with *log v*. The slope of the linear correlation is 0.58 for the NPG microelectrode prepared at t_D = 100 s, which is expected for a predominately diffusion step. However, for t_D = 200 s, two different slopes are obtained in agreement with the E_p vs. *log v* plot. At lower scan rates, the slope is ca. 0.53, which corresponds to a mass transport process, while at higher scan rates, the slope is 0.84, which indicates the prevalence of an adsorption process. At higher t_D values (400 s and 600 s), the slopes are closer to ca. 0.8, indicating a mixed process with a significant adsorption contribution.

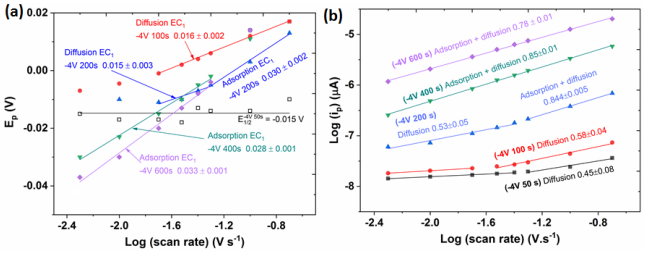

Figure 7. Plots of E_p vs. log (scan rate) (a) and log (i_p) vs. log (scan rate) (b) at different NPG microelectrodes prepared at fixed E_D (-4 V) for different t_D (50, 100, 200, 400, and 600 s), extracted from CVs recorded in 0.1 mmol L^{-1} AA +0.1 mol L^{-1} PBS. Slopes are indicated in the graph.

The transition from a *diffusion EC₁* to an *adsorption EC₁* process as a function of t_D for the NPG microelectrode can be linked to the film pore size, which can be tuned by changing the experimental conditions. For instance, NPG films grown by DHBT deposition present larger pores as the deposition time increases, as shown in Fig. 2. At such NPG platforms prepared at longer t_D values (400 and 600 s), AA from the bulk can diffuse deeper within the film volume. Hence, this increases the interaction with the porous walls and enhances the adsorption, which results in the *adsorption EC₁* mechanism. It is also evident from SEM images (Fig. 2) that the morphology of NPG films prepared at shorter t_D values is denser and the surface pores are smaller in size, which induces significant mass transport limitation for AA diffusion within the film volume.

Conclusion

In this work, we have demonstrated that mass transport and the preferred reaction pathways of AA electrode processes at NPG surfaces are strongly correlated with the film porosity. Different NPG microelectrodes were synthesized by the DHBT method changing electrodeposition parameters (potential and time) in a controlled manner. The NPG films were characterized by CV, XRD, and electron microscopy techniques, and the results revealed a pure gold polycrystalline film of very high surface area and diverse porosity. The porosity and the electrochemical surface area of the NPG films depend on both E_D and t_D, such that an increase in t_D induces the formation of larger surface pores with increased electrochemical surface area according to an exponential growth model. Similar behavior was noticed by making E_D more negative, and denser films and a linear increase in the electrochemical surface area were observed. The investigation of the AA electrochemical processes at the NPG microelectrodes revealed faster reaction kinetics and strong electrocatalysis, evidenced by the sharp voltammetric curve and a shift of more than 400 mV in the oxidation peak towards less positive values compared to the same process at the bare gold microelectrode. However, the associated reaction paths at different NPG microelectrodes were different, following predominately either *diffusion EC₁* or *adsorption EC₁* processes. NPG microelectrodes prepared at varying E_D for a short fixed t_D always revealed a *diffusion EC₁* process. On the other hand, NPG microelectrodes prepared at different t_D for a fixed E_D exhibited a *diffusion EC₁* process at shorter times, a combination of diffusion and adsorption processes at intermediate times, and dominantly an *adsorption EC₁* process at longer times. Such transition from a *diffusion EC₁* into an *adsorption EC₁* mechanism was correlated with the NPG surface pore features. Hence, larger pores are generated at longer t_D values, allowing AA to diffuse within the NPG film volume and thus enhancing the adsorption probability.

Experimental Section

Materials and reagents. All chemicals used in this work were of analytical grade and were used without any further purifications. L-ascorbic acid ($C_6H_8O_6$, Molecular weight: 176.12 g mol^{-1}, ≥ 99%), gold(III) chloride trihydrate (Molecular weight: 393.83 g mol^{-1}, $HAuCl_4 \cdot 3H_2O$, ≥ 99.9%) and phosphate buffer saline (PBS) tablets were procured from Sigma-Aldrich. Milli-Q ultrapure water (resistivity ~18 MΩ cm) was used to prepare all aqueous solutions. PBS buffer solution of pH~7.4 was prepared by dissolving one commercial tablet in 200 mL water, which was also used to prepare the ascorbic acid stock solution (0.1 mol L^{-1}).

Electrochemical setup. Electrochemical measurements were performed with PGSTAT-128N and PGSTAT-320N Autolab Metrohm workstations interfaced with Nova 1.11 software. A conventional three-electrode cell comprising NPG modified gold, Ag/AgCl (KCl sat.), and platinum as working, reference, and counter electrodes, respectively, was used in the electrochemical experiments. In-house fabricated gold microelectrode (size: 50 μm) was used as a working electrode and as substrate to prepare NPG films (Fabrication procedure in SI). The electrode surface was cleaned at first by polishing with alumina slurry followed by electrochemical CV cycling in 0.5 mol L^{-1} H_2SO_4 in the range of -0.4 to 1.6 V at the scan rate of 50 mV s^{-1}. All electrochemical experiments involving NPG microelectrodes were performed by CV in deoxygenated 0.1 mol L^{-1} PBS. The potential window and scan rate range were selected between -0.5 to 0.6 V and 5 to 200 mV s^{-1}.

Electrodeposition of NPG and electrochemical characterization. NPG films were deposited on the gold microelectrode by the DHBT method in a strongly stirred 5 mmol L^{-1} $HAuCl_4$ in 0.5 mol L^{-1} H_2SO_4 solution. The deposition was performed potentiostatically at a fixed applied potential (E_D) for a given time (t_D). Two sets of NPG films were electrodeposited (a) at E_D = -1.0 V, -2.0 V, -3.0 V, and -4.0 V for t_D = 100 s and (b) at E_D = -4.0 V for t_D = 50 s, 100 s, 200 s, 400 s, and 600 s. After the electrodeposition, the films were washed with distilled water and air-dried at room temperature. The electrodeposition procedure was performed at room temperature in the absence of any external gas bubbling. After each electrodeposition, a CV of the NPG microelectrode was recorded in 0.5 mol L^{-1} H_2SO_4 at a scan rate of 50 mV s^{-1} in the 0.2 to 1.6 V range.

Structural and morphological characterization. The NPG film´s surface morphology was examined using a JEOL JSM-FEG 7401F SEM by scanning the surface at an accelerating voltage of 2 kV. ImageJ software was used to assess the distribution of pore sizes, length of the fractals, and scaling of the images. The chemical purity of the NPG films was estimated by performing XPS on SIA100 spectrometer (Cameca Riber apparatus) using Al Kα X-ray source (1486.6 eV photons). The crystalline structure of the NPG films was studied using the Selected Area Electron Diffraction (SAED) pattern, recorded in a High-Resolution Transmission Electron Microscopy (HRTEM) imaging mode (sample preparation procedure in SI). The experiments were performed on a JEOL JEM-2100 microscope equipped with a Field Emission Gun (FEG, ZrO/W(100)), Schottky field emission electron source) operating at 200 kV. The point resolution of the instrument was 0.19 nm. NPG films were characterized by XRD using a tabletop Bruker D2 Phaser X-ray diffractometer to determine the crystallographic orientation. The instrument was equipped with a Cu Kα source (λ = 1.5418 Å). The experiments were carried out in the 2θ window of 10 to 90°, using a scan step of 0.05º and at room temperature.

Acknowledgements

The authors are thankful to Sao Paulo Research Foundation (FAPESP) (2016/07461-1, 2017/13137-5 and 2018/08782-1) and National Council for Scientific and Technological Development (CNPq 311847-2018-8, 442599/2019-6, 303137/2016-9). Authors would also like to thank for receiving financial support from Université de Bourgogne and European Union through PO FEDER-FSE Bourgogne 2019/2022 (via CoMICS program) and BQR program (A.K.), Agence Nationale de la Recherche (ANR) (OUTSMART ANR-2015-CE39-0004-03) and Conseil Régional de Bourgogne (CPER program). The LNNano, CNPEM, Campinas are thanked for allowing the use of electron microscopy facilities.

O. Heintz and A. Krystianiak are acknowledged for performing XPS measurements.

Keywords: Nanoporous gold • Mass transport • Microporous materials • Electrochemistry • EC_1 reaction

[1] a) M. Dabrowski, M. Cieplak, P. S. Sharma, P. Borowicz, K. Noworyta, W. Lisowski, F. D'Souza, A. Kuhn, W. Kutner, *Biosens. Bioelectron.* **2017**, *94*, 155-161; b) P. N. Bartlett, M. A. Ghanem, I. S. El Hallag, P. de Groot, A. Zhukov, *J. Mater. Chem.* **2003**, *13*, 2596-2602.

[2] a) A. Walcarius, A. Kuhn, *TrAC Trends in Anal. Chem.* **2008**, *27*, 593-603; b) A. Walcarius, *Chem. Soc. Revi.* **2013**, *42*, 4098-4140; c) A. Andrieu-Brunsen, S. Micoureau, M. Tagliazucchi, I. Szleifer, O. Azzaroni, G. J. A. A. Soler-Illia, *Chem. Mater.* **2015**, *27*, 808-821.

[3] B. Jiang, Y. Guo, J. Kim, A. E. Whitten, K. Wood, K. Kani, A. E. Rowan, J. Henzie, Y. Yamauchi, *J. Am. Chem. Soc.* **2018**, *140*, 12434-12441.

[4] a) L. C. Nagle, J. F. Rohan, *Int. J. Hydrogen Energy* **2011**, *36*, 10319-10326; b) S.-I. Kim, S.-W. Kim, K. Jung, J.-B. Kim, J.-H. Jang, *Nano Energy* **2016**, *24*, 17-24; c) J. van der Zalm, S. Chen, W. Huang, A. Chen, *J. Electrochem. Soc.* **2020**, *167*, 037532; d) L. Y. Chen, T. Fujita, M. W. Chen, *Electrochim. Acta* **2012**, *67*, 1-5.

[5] A. Wittstock, A. Wichmann, J. Biener, M. Bäumer, *Faraday Discuss.* **2011**, *152*, 87-98.

[6] a) Y. Ding, Y. J. Kim, J. Erlebacher, *Adv. Mater.* **2004**, *16*, 1897-1900; b) A.-A. El Mel, F. Boukli-Hacene, L. Molina-Luna, N. Bouts, A. Chauvin, D. Thiry, E. Gautron, N. Gautier, P.-Y. Tessier, *ACS Appl. Mater. Interfaces* **2015**, *7*, 2310-2321; c) A. Lackmann, M. Bäumer, G. Wittstock, A. Wittstock, *Nanoscale* **2018**, *10*, 17166-17173.

[7] H. C. Shin, J. Dong, M. Liu, *Adv. Mater.* **2003**, *15*, 1610-1614.

[8] A. Kumar, J. M. Gonçalves, A. Sukeri, K. Araki, M. Bertotti, *Sens. Actuators, B* **2018**, *263*, 237-247.

[9] F. Jia, C. Yu, K. Deng, L. Zhang, *J. Phys. Chem. C* **2007**, *111*, 8424-8431.

[10] B. Seo, J. Kim, *Electroanalysis* **2010**, *22*, 939-945.

[11] a) J. Biener, M. M. Biener, R. J. Madix, C. M. Friend, *ACS Catal.* **2015**, *5*, 6263-6270; b) T. Fujita, P. Guan, K. McKenna, X. Lang, A. Hirata, L. Zhang, T. Tokunaga, S. Arai, Y. Yamamoto, N. Tanaka, Y. Ishikawa, N. Asao, Y. Yamamoto, J. Erlebacher, M. Chen, *Nat. Mater.* **2012**, *11*, 775-780.

[12] a) J. H. Bae, J.-H. Han, D. Han, T. D. Chung, *Faraday Discuss.* **2013**, *164*, 361-376; b) J.-H. Han, E. Lee, S. Park, R. Chang, T. D. Chung, *J. Phys. Chem. C* **2010**, *114*, 9546-9553.

[13] X. Ge, L. Wang, Z. Liu, Y. Ding, *Electroanalysis* **2011**, *23*, 381-386.

[14] a) A. Kumar, J. S. G. Selva, J. M. Gonçalves, K. Araki, M. Bertotti, *Electrochim. Acta* **2019**, *322*, 134772; b) H. S. C. Sáenz, L. P. Hernández-Saravia, J. S. G. Selva, A. Sukeri, P. J. Espinoza-Montero, M. Bertotti, *Microchim. Acta* **2018**, *185*, 367.

[15] C. W. Bae, P. T. Toi, B. Y. Kim, W. I. Lee, H. B. Lee, A. Hanif, E. H. Lee, N.-E. Lee, *ACS Appl. Mater. Interfaces* **2019**, *11*, 14567-14575.

[16] N. Li, C. Nan, X. Mei, Y. Sun, H. Feng, Y. Li, *Microchim. Acta* **2020**, *187*, 496.

[17] A. Kumar, V. L. Furtado, J. M. Gonçalves, R. Bannitz-Fernandes, L. E. S. Netto, K. Araki, M. Bertotti, *Anal. Chim. Acta* **2020**, *1095*, 61-70.

[18] N. Smirnoff, *Free Radical Biol. Med.* **2018**, *122*, 116-129.

[19] a) K. Dhara, R. M. Debiprosad, *Anal. Biochem.* **2019**, *586*, 113415; b) A. M. Pisoschi, A. Pop, A. I. Serban, C. Fafaneata, *Electrochim. Acta* **2014**, *121*, 443-460.

[20] a) P. Karabinas, D. Jannakoudakis, *J. Electroanal. Chem. Interfacial Electrochem.* **1984**, *160*, 159-167; b) M. Rueda, A. Aldaz, F. Sanchez-Burgos, *Electrochim. Acta* **1978**, *23*, 419-424.

[21] J. Wang, B. A. Freiha, *Talanta* **1983**, *30*, 317-322.

[22] X. Xing, M. Shao, M. W. Hsiao, R. R. Adzic, C.-C. Liu, *J. Electroanal. Chem.* **1992**, *339*, 211-225.

[23] L. Zhang, F. Liu, X. Sun, G.-f. Wei, Y. Tian, Z.-p. Liu, R. Huang, Y. Yu, H. Peng, *Anal. Chem.* **2017**, *89*, 1831-1837.

[24] G. Hu, Y. Ma, Y. Guo, S. Shao, *Electrochim. Acta* **2008**, *53*, 6610-6615.

[25] a) J. Yan, S. Liu, Z. Zhang, G. He, P. Zhou, H. Liang, L. Tian, X. Zhou, H. Jiang, *Colloids Surf., B* **2013**, *111*, 392-397; b) X. Zhang, S. Yu, W. He, H. Uyama, Q. Xie, L. Zhang, F. Yang, *Biosens. Bioelectron.* **2014**, *55*, 446-451.

[26] a) W. A. El-Said, J.-H. Lee, B.-K. Oh, J.-W. Choi, *Electrochem. Commun.* **2010**, *12*, 1756-1759; b) H.-J. Qiu, G.-P. Zhou, G.-L. Ji, Y. Zhang, X.-R. Huang, Y. Ding, *Colloids Surf., B* **2009**, *69*, 105-108; c) T. A. Silva, M. R. K. Khan, O. Fatibello-Filho, M. M. Collinson, *J. Electroanal. Chem.* **2019**, *846*, 113160.

[27] A. Kumar, J. M. Gonçalves, J. S. G. Selva, K. Araki, M. Bertotti, *J. Electrochem. Soc.* **2019**, *166*, H704-H711.

[28] a) J. W. Haverkort, *Electrochim. Acta* **2019**, *295*, 846-860; b) S. Park, Y. J. Song, J.-H. Han, H. Boo, T. D. Chung, *Electrochim. Acta* **2010**, *55*, 2029-2035.

[29] J. Veselinovic, S. AlMashtoub, S. Nagella, E. Seker, *Anal. Chem.* **2020**, *92*, 10751-10758.

[30] M. Haensch, L. Balboa, M. Graf, A. R. Silva Olaya, J. Weissmüller, G. Wittstock, *ChemElectroChem* **2019**, *6*, 3160-3166.

[31] a) C. Karman, N. Vilà, A. Walcarius, *ChemElectroChem* **2016**, *3*, 2130-2137; b) P. Audebert, N. Vilà, C. Allain, F. Maisonneuve, A. Walcarius, P. Hapiot, *ChemElectroChem* **2015**, *2*, 1695-1698; c) A. Andrieu-Brunsen, S. Micoureau, M. Tagliazucchi, I. Szleifer, O. Azzaroni, G. J. A. A. Soler-Illia, *Chem. Mater.* **2015**, *27*, 808-821.

[32] B. J. Plowman, L. A. Jones, S. K. Bhargava, *Chem. Commun.* **2015**, *51*, 4331-4346.

[33] a) A. Hamelin, *J. Electroanal. Chem.* **1996**, *407*, 1-11; b) C. Jeyabharathi, P. Ahrens, U. Hasse, F. Scholz, *J. Solid State Electrochem.* **2016**, *20*, 3025-3031.

[34] M. S. El-Deab, *Electrochim. Acta* **2009**, *54*, 3720-3725.

[35] H. E. M. Hussein, R. J. Maurer, H. Amari, J. J. P. Peters, L. Meng, R. Beanland, M. E. Newton, J. V. Macpherson, *ACS Nano* **2018**, *12*, 7388-7396.

[36] T. A. Witten, L. M. Sander, *Phys. Rev. Lett.* **1981**, *47*, 1400-1403.

[37] L. Soleymani, Z. Fang, E. H. Sargent, S. O. Kelley, *Nat. Nanotechnol.* **2009**, *4*, 844-848.

[38] Y. Qin, Y. Song, N. Sun, N. Zhao, M. Li, L. Qi, *Chem. Mater.* **2008**, *20*, 3965-3972.

[39] F. Prieto, B. A. Coles, R. G. Compton, *J. Phys.Chem. B* **1998**, *102*, 7442-7447.

[40] E. Laviron, *J. Electroanal. Chem.* **1995**, *391*, 187-197.

[41] J. M. Savéant, J. *Electroanal. Chem. Interfacial Electrochem.* **1980**, *112*, 175-188.

[42] E. Laviron, *J. Electroanal. Chem. Interfacial Electrochem.* **1972**, *35*, 333-342.
[43] R. S. Nicholson, I. Shain, *Anal. Chem.* **1964**, *36*, 706-723.
[44] M. Mastragostino, L. Nadjo, J. M. Saveant, *Electrochim. Acta* **1968**, *13*, 721-749.
[45] J.-M. Savéant, *Coupling of Electrode Electron Transfers with Homogeneous Chemical Reactions*, John Wiley & Sons, Inc., Hoboken, New Jersey, **2019**.